BLADE TWIST EFFECTS ON HOVERING TILT ROTOR FLOW FIELDS

Gloria K. Yamauchi

Aerospace Engineer
NASA Ames Research Center, Moffett Field, CA

and

Wayne Johnson
Johnson Aeronautics, Palo Alto, CA

SUMMARY

The flow field of highly-twisted rotors in hover was analyzed using a thin-layer Navier-Stokes analysis. The objective of the investigation was to understand how various fluid dynamic phenomena affect tilt rotor hover performance and how these phenomena differ for a conventional helicopter blade, especially near stall conditions. Differences in rotor performance, blade loads, skin friction, flow separation location, and flow field vorticity were investigated at near-stall conditions as the blade twist was systematically changed from that of a tilt rotor (full-scale V-22) to a rotor with a linear twist. Starting with an existing Navier-Stokes analysis for hovering helicopter rotors, boundary conditions at the blade root and far-field were modified. A no-slip boundary condition at the blade root and a far-field inflow boundary condition based on mass conservation were implemented. These modifications produced noticeable effects on calculated section loads and performance. As the twist was changed from a tilt rotor blade twist to a conventional helicopter blade twist, while maintaining thrust, the separated region near the tip grew. This caused the section in-plane force near the tip to increase significantly, which caused the rotor torque to increase, finally resulting in degraded performance. The flow in the blade inboard region ($r/R < 0.50$) remained attached and well-behaved for all twist cases and thrust conditions analyzed. The calculations indicated that separation on the linearly twisted blade was closely coupled with the tip vortex, while separation on the tilt rotor blade was shock-induced. In addition, the study showed that twist distributions with more inboard twist than the V-22 can provide better hover performance.

NOTATION

a_∞	free stream sound speed
c	chord
c_{ref}	reference chord, chord at 0.75 radial station
C_n	section normal force/$(0.5\rho_\infty(\Omega r)^2 c)$
C_q	section torque/$(0.5\rho_\infty(\Omega R)^2 R c_{ref})$
C_t	section thrust/$(0.5\rho_\infty(\Omega R)^2 c_{ref})$
C_x	section in-plane force/$(0.5\rho_\infty(\Omega R)^2 c_{ref})$
C_Q	rotor torque/$(\pi R^3 \rho_\infty(\Omega R)^2)$
C_T	rotor thrust/$(\pi R^2 \rho_\infty(\Omega R)^2)$
FM	figure of merit, $\dfrac{C_T^{1.5}}{\sqrt{2}C_Q}$
M_{tip}	blade tip Mach number, $\Omega R/a_\infty$
p_∞	free stream static pressure
r	blade radial coordinate, radial location/R
R	blade radius
Re	Reynolds number, $\Omega R c_{ref}/\nu_\infty$
x,y,z	inertial coordinates
u,v,w	nondimensional inertial space velocities

488

ρ	density
ρ_∞	free stream density
Ω	rotor speed
$\xi,\eta,\zeta,$	blade-fixed computational coordinates

INTRODUCTION

The concept of tilt rotor aircraft is not new, and after years of design work, wind tunnel testing, flight testing, and political indecision, the production of tilt rotor aircraft for the military finally seems assured. Despite the long history of tilt rotors, however, the ability of the research community to analyze the various aerodynamic and acoustic phenomena particular to these aircraft is not considered adequate. To be fair, aeroacoustic predictions for conventional helicopters are not considered exceptional either, although much more work has been done both experimentally and analytically for helicopter rotors than tilt rotors.

Aside from the obvious physical differences between a tilt rotor aircraft and conventional helicopter, limited experimental data have revealed differences in rotor wake geometry, blade loading, and hover performance. In particular, for the same mean blade lift at high thrust levels, a tilt rotor will provide better hover performance than a helicopter rotor. The difference in hover performance between the two aircraft can be directly attributed to the differences in rotor blade geometry. The tilt rotor blade has a smaller aspect ratio (approximately 60% of a helicopter blade), taper from root to tip (helicopter blades usually only have taper near the tip), thicker airfoils (on the order of 30% thick at the root), and a nonlinear twist distribution with extremely high twist at the blade root (in contrast, a conventional helicopter blade has a low, linear twist over the majority of the blade span). The physical differences are required since the tilt rotor blade experiences flow regimes including hover, helicopter or edgewise flight, and axial flight. Therefore, the blade must include characteristics of a helicopter and propeller blade. The difficult question to answer is how these physical features combine to influence the blade fluid dynamic environment which then provides a noticeable improvement in hover performance compared to the helicopter rotor. This is the focus of the present investigation. Before proceeding, a brief review of the more recent computational work in hover performance is presented in order to establish the context in which the present investigation is conducted.

Most CFD rotor analyses evolved from fixed-wing analyses and were initially full-potential (for example, Strawn and Caradonna (Ref. 1)) and Euler formulations (for example, Chen, McCroskey, and Ying (Ref. 2)) before the arrival of thin-layer, Navier-Stokes analyses. Also, the CFD rotor analyses initially relied on external analyses to provide the wake effects (for example, Srinivasan and McCroskey (Ref. 3) and Narramore and Vermeland (Ref. 4)).

A complete three-dimensional, viscous, and compressible rotor flow field analysis which included a rotor wake was presented by Srinivasan, Baeder, Obayashi, and McCroskey (Ref. 5). The analysis was named Transonic Unsteady Rotor Navier-Stokes or TURNS. Limited hover performance predictions with this analysis were presented by Srinivasan, Raghavan, and Duque (Ref. 6) for a model UH-60A rotor. At high thrust levels, discrepancies in figure of merit were approximately four percent. Blade surface pressures, section thrust distribution, and rotor wake geometry predictions were in generally good agreement with measurements. Wake and Baeder (Ref. 7) used this same analysis to perform a more in-depth correlation study with the model-scale UH-60A data. The authors concluded that although the analysis can be used to examine flow field details, performance predictions were not better than those computed by simpler lifting-line analyses. Tung and Lee (Ref. 8) evaluated the three most promising hover performance codes at the time, HELIX, EHPIC, and TURNS, by comparing calculated surface pressures and performance values with the data from the small-scale UH-60A rotor with three different tips. EHPIC was determined to provide the best overall correlation results of the three analyses, although EHPIC did not model stall effects. Ramachandran, Owen, Caradonna, and Moffitt (Ref. 9) presented more detailed comparisons of HELIX calculations with the UH-60A small-scale data. Surface pressure comparisons were good, as were performance comparisons, as long as attached flow conditions were being simulated. Meakin (Ref. 10) simulated a V-22 rotor and wing in hover using the thin-layer, Navier-Stokes solver OVERFLOW and multiple overset grids moving in relative motion. Good agreement with measured wing surface pressure data was obtained for one condition. Using the sophisticated gridding methodology of Meakin (Ref. 10) to pursue hover performance prediction for the tilt rotor should serve as an interesting follow-on study.

Despite the increased sophistication of numerical schemes and grid generation techniques, no state-of-the-art analysis is able to predict hover performance, especially at high thrust levels, to within the 1 percent desired by designers (Kocurek, Harris, Berkowitz (Ref. 11)). To reach this level of accuracy may require implementing some or all of the following: higher-order differencing schemes, higher-order metric evaluation, extremely dense grids concentrated along the paths of the tip vortices, overset grids (including unstructured grids), improved turbulence models, etc. Since hovering tilt rotors operate at higher thrust levels than hovering helicopter rotors, predicting tilt rotor performance is even more problematic since stall may occur under these

489

high loading conditions. In addition, experimental evidence shows that tilt rotors and helicopter rotors perform differently at high thrust, suggesting that the stall behavior of tilt rotors and helicopter rotors involves different phenomena. Currently, computational analyses originally developed for helicopter rotors are being used to model tilt rotor geometries. The geometry and flow conditions of tilt rotor blades can easily test the limitations of these analyses. Experimental evidence (different performance at high thrust) and theoretical evidence (different accuracy of predictive methods) show that the stall behavior of helicopter rotors and tilt rotors must be phenomenologically different.

The objective of this work is to understand how various fluid dynamic phenomena interact and how this interaction ultimately affects tilt rotor hover performance. The objective is not to improve the performance prediction capability, since this will probably require advances in all of the areas mentioned above. Identifying how the tilt rotor blade fluid dynamic environment differs from that of a conventional rotor blade sheds light on the events leading up to stall, which seriously impacts performance. As highlighted earlier, one of the key physical differences between a tilt rotor and helicopter blade is the built-in twist. The significant difference in blade twist is used as the focal point of this study. Differences in flow separation location, tip vortex formation, and other fluid dynamic phenomena are investigated as the blade twist is systematically changed from that of a tilt rotor to a linear twist. Based on these results, major differences between the behavior of tilt rotor blades and conventional helicopter blades can be isolated.

The analysis chosen as a starting point for the present study was TURNS. TURNS was selected since the analysis has been demonstrated to sufficiently predict conventional helicopter flow field parameters. Also, Yamauchi and Johnson (Ref. 12) demonstrated that the analysis was appropriate for investigating the flow field of a model prop rotor. In addition, since boundary layer parameters such as skin friction will be investigated in this study, a viscous analysis was required.

This study begins by describing the TURNS analysis. The numerical solution and computational grid are described next. Boundary conditions are discussed in detail, including the implementation of major modifications in the original TURNS analysis. The effects of these modifications are presented and discussed. The study of twist effects is performed using a V-22 blade geometry. Twist effects are studied by systematically reducing the V-22 blade twist to that of a linearly twisted blade, while maintaining the same airfoils and blade planform. A comprehensive description of the changes in flow field details is provided. Finally, specific findings from the investigation are summarized.

ANALYSIS DESCRIPTION

The analysis solves the thin-layer Navier-Stokes equations cast in a general nonorthogonal coordinate system (Pulliam and Steger (Ref. 13)),

$$\partial_\tau \widehat{Q} + \partial_\xi \widehat{E} + \partial_\eta \widehat{F} + \partial_\zeta \widehat{G} = \frac{1}{Re} \partial_\zeta \widehat{S} \qquad (1)$$

where

$$Q = [\, \rho \;\; \rho u \;\; \rho v \;\; \rho w \;\; e \,]^T \;,\; \widehat{Q} = Q/J \qquad (2)$$

$\widehat{E}, \widehat{F}, \widehat{G}$ are the convective flux vectors and $\widehat{S}$ is the viscous flux vector using the thin-layer approximation. The flux vectors have been normalized by the Jacobian J. The velocity components in the Cartesian inertial frame are represented by u, v, and w. The density, mass fluxes, and energy per unit volume are nondimensionalized by the far-field reference quantities. The Reynolds number, Re, is based on M_{tip} and a reference chord (defined as the chord at 0.75R for this investigation). The reference chord and sound speed are the characteristic length and velocity scales, respectively. The equation of state for a perfect gas and Eq. 1 describe the entire flow field. The blade-fixed computational coordinates (Fig. 1) are defined by (ξ,η,ζ); the curvilinear coordinate system is fixed relative to the blade surface.
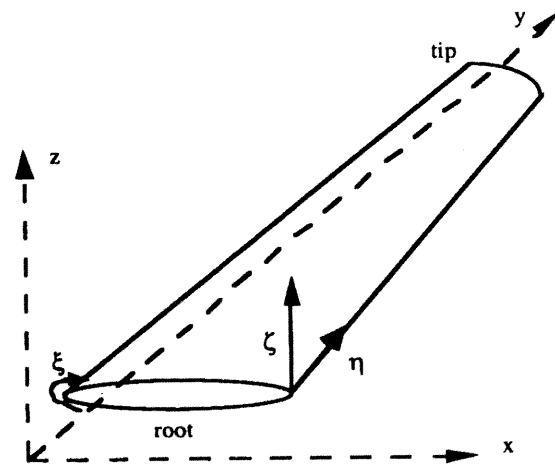

Figure 1. Curvilinear coordinate system.

NUMERICAL SOLUTION

The solution procedure used in this investigation evolved from numerical schemes and techniques originally

used to solve fixed-wing problems. Modifications to a fixed-wing analysis were made by Srinivasan during a series of studies investigating tip-vortex formation on fixed-wings with different tips (Srinivasan, McCroskey, Baeder, and Edwards (Ref. 14)). The analysis was further modified to calculate rotor flows in hover and forward flight (Srinivasan and McCroskey (Ref. 3) and Srinivasan and McCroskey (Ref. 15)); rotor wake effects, however, were computed by a separate analysis. In 1990, Srinivasan et al (Ref. 5) incorporated major modifications to the analysis which included upwinding for all three (instead of just one) coordinate directions. The upwinding scheme was adapted from the work of Obayashi (Ref. 16). Source terms, to calculate the flow in the blade-fixed coordinate system, and wake capturing features were also included which eliminated the need for an external wake calculation. As described in Srinivasan et al (Ref. 5), the right-hand side of Eq. 1 (after discretization) employed the upwind-biased, flux-difference splitting scheme; a Lower-Upper-Symmetric Gauss-Seidel (LU-SGS) scheme was used for the implicit operator. A monotone upstream-centered scheme for conservative laws (MUSCL) was used to achieve 2nd- or 3rd-order spatial accuracy with flux limiters. In the present study, the solution was 3rd-order accurate in the ξ-direction, and 2nd-order accurate in the η- and ζ-directions. The space metrics were evaluated using a finite volume formulation, while a finite difference formulation is used for the time metrics. The turbulence model used was the Baldwin-Lomax model. This modified version of the flow solver was named the Transonic Unsteady Rotor Navier-Stokes (TURNS) code. TURNS was the analysis used as a starting point for the present investigation.

COMPUTATIONAL GRID

The computational grid used in this study was a three-dimensional C-H grid composed of stacked two-dimensional C-grids. The C-grids conform to the blade surface; aft of the blade trailing edge at each spanwise station, the grid collapsed to a slit. At the blade tip, the grid again collapsed to a slit, resulting in a beveled tip. The outer grid was adjusted and smoothed to accommodate the periodic boundary condition which required the front and back of the outer grid to match. The baseline grid size was 181x49x49, defined as 181 points in the wrap-around (or ξ-) direction, 49 points in the spanwise (or η-) direction, and 49 points in the normal (or ζ-) direction (Fig. 1). Of the 181 points in the wrap-around direction, 145 defined the blade profile; 30 of the 49 grid stations in the spanwise direction defined the blade from root to tip. The outer boundaries were one rotor diameter above and below the rotor plane. The distance to the first point off the blade surface in the normal direction was 0.00004 c_{ref} (chord at 0.75R). Yamauchi and Johnson (Ref. 17) determined this value to be sufficient for defining the velocity profile in the boundary layer for a highly-twisted rotor. Also, Yamauchi and Johnson (Ref. 17) found that precone had minimal effect on the performance and loads of a

V-22 blade; therefore, precone was neglected in the present investigation. The spanwise location of the outer boundary was one rotor radius beyond the blade tip. The blade surface grid is shown in Fig. 2a), while a spanwise cut of the entire grid is shown in Figs. 2b) and c) for radial stations 0.23 and 0.95, respectively. The collective pitch (mean geometric blade pitch, measured at 75 percent radial station, used to control rotor thrust) for Fig. 2 is 16 degrees.

Since this investigation concentrated on highly twisted rotors, the periodic boundary condition resulted in blade sectional grids which were twisted and skewed. Also, to achieve the high thrust levels required for studying stall and flow separation, a large collective pitch was imposed resulting in a very high geometric pitch angle at the blade root, which sometimes caused highly distorted grid cells resulting in negative Jacobians. For this reason, the first airfoil section of the blade grid was located farther outboard (0.23R) compared to the actual blade (0.09R). Adjustments to grid spacing were tuned to avoid negative Jacobians, although only a limited amount of grid parameter variations were possible using these highly skewed grids. For example, the spacing near the blade surface, root, and trailing edge could not be widely varied before encountering problems for the high collective pitch cases. However, an adequate number of grid parameter variations, in addition to a grid density study, were performed to establish confidence in the baseline grid size (Yamauchi (Ref. 18)).

BOUNDARY CONDITIONS

At the blade surface, a no-slip condition was used with a finite velocity due to blade rotation. The surface pressure was obtained through the normal momentum equation and the density was evaluated by the adiabatic wall condition. Since the hover condition was assumed to be steady and symmetric for this study, a periodic flow condition was used in the azimuthal direction; therefore, only one blade was modeled. The blade root and far-field boundary conditions are discussed in the following sections.

Blade Root

In Srinivasan et al (Ref. 5), the inertial velocity components at the blade root plane were obtained by assuming a zero velocity gradient in the spanwise direction. This boundary condition, although acceptable at the centerline of a fixed-wing, is not appropriate for a rotor blade. Therefore, in this investigation, the root plane boundary was modified to be more representative of a rotor blade and center body. The center body was assumed to rotate with the blade, similar to a tilt rotor blade and spinner, thereby forming a no-flow-through surface. A no-slip condition at the root plane was selected over an Euler condition since applying the no-slip condition from the blade surface to the root plane was fairly straightforward. Using the no-slip condition was not expected to provide noticeable differences in results

leading edge

root
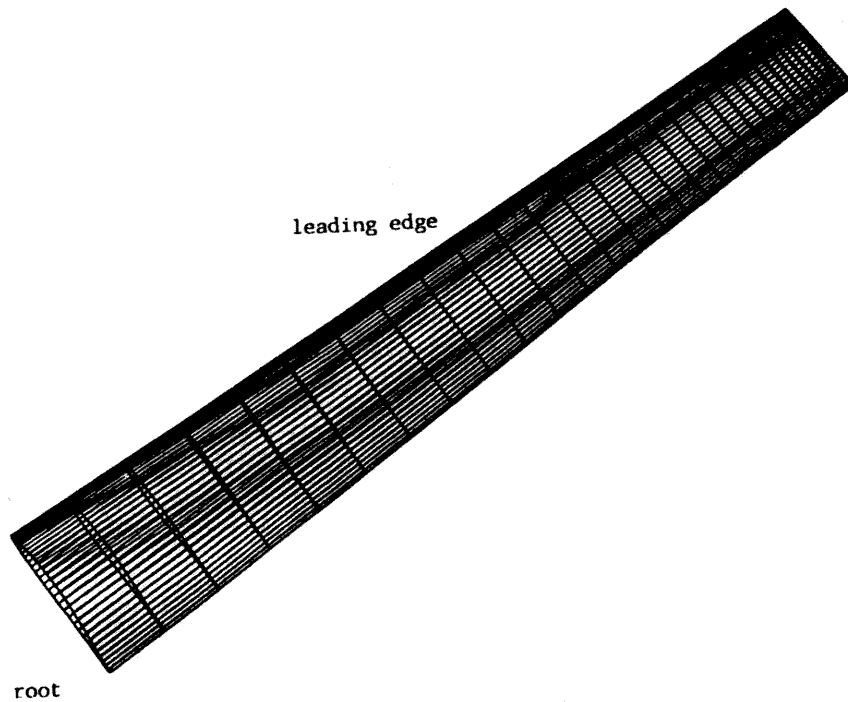
a) surface grid (every other point in the chordwise direction shown for clarity)
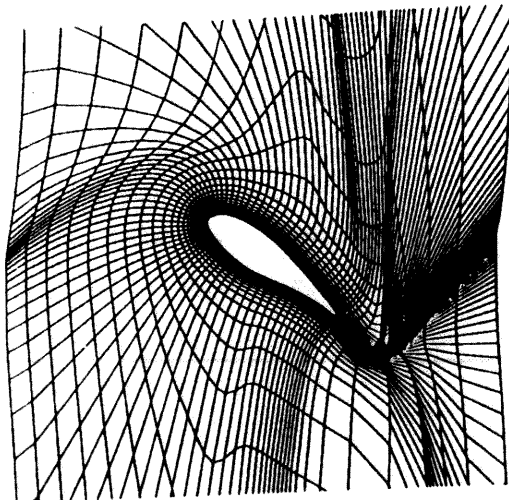
b) section grid at r/R=0.23
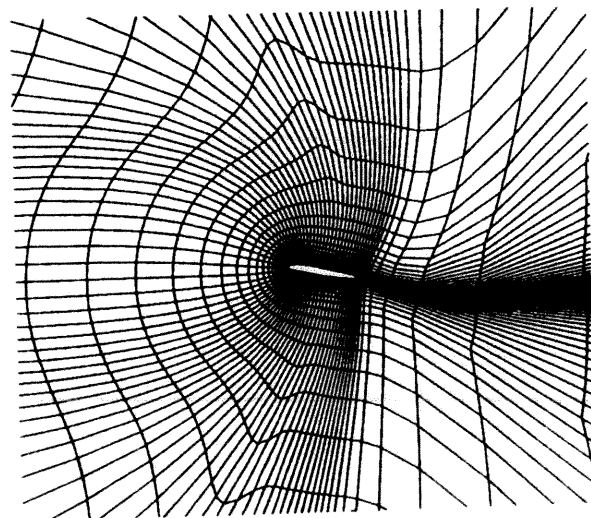
c) section grid at r/R=0.95

Figure 2. Surface and sectional grids for the V-22 blade for a collective pitch of 16 deg every other grid point shown for clarity).

compared to an Euler condition for the reasons discussed below.

Pulliam and Steger (Ref. 13) state that if a vertical and horizontal wall are being analyzed with the thin-layer equations, the walls should be treated as a single surface, otherwise, the neglected viscous terms in the spanwise direction (for the vertical wall) should be added. This approach was used in Fuji and Obayashi (Ref. 19) in the analysis of the viscous flow over a wing-fuselage combination. However, the neglected terms in the η-(spanwise) direction were not included in the present study for several reasons. First, the objective was to simulate a no-flow-through surface at the root and not to capture viscous behavior at the blade-root juncture. Second, even if the extra terms were added, the grid spacing in the spanwise direction must be greatly refined near the root in order to capture any boundary layer formation. This was not possible with the current grid generator and the large blade root twist being studied. Therefore, the modification made was considered a justified compromise between the original boundary condition implementation at the root and the procedure used by Fuji and Obayashi (Ref. 19).

Far-Field

The computational domain extended one rotor radius beyond the blade tip and one rotor diameter above and below the rotor plane. For this domain size, approximations were required at the far-field boundaries to prevent flow recirculation. These approximations are discussed in this section.
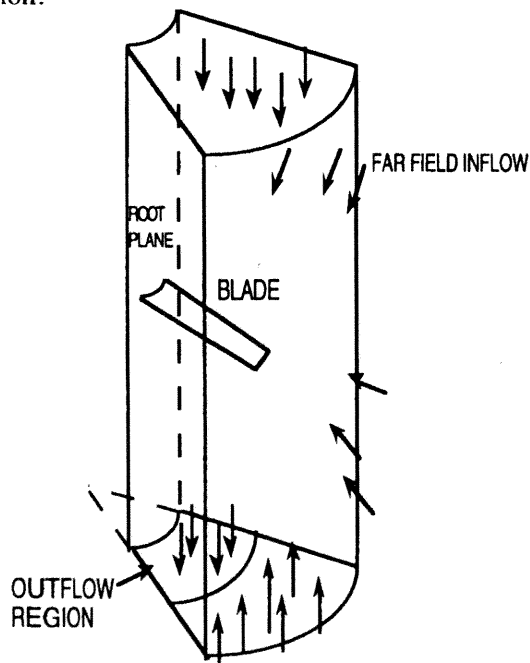
Figure 3. Outflow and inflow boundaries.

As depicted in Fig. 3, the flow exits through a bottom boundary and enters the computational domain everywhere else at the outer boundary. Srinivasan et al (Ref. 6) approximated the inflow velocity at the outer boundaries by assuming a three-dimensional sink at the center of rotation; the sink strength was determined from the rotor thrust using momentum theory. At the bottom boundary, the flow exits through an area one-half the rotor disk area. The exit velocity was prescribed to be uniform and twice the momentum theory value at the rotor plane. Srinivasan et al (Ref. 6) reported that implementing this inflow boundary condition prevented recirculation in the computational domain. Strawn and Barth (Ref. 20) enhanced the method of Srinivasan et al (Ref. 6) by enforcing mass conservation through the computational domain by superposing the inflow velocity and the exit velocity at the lower boundary.

A different approach was used in the present study. Instead of using momentum theory to prescribe the exit velocity at the lower boundary, the exit velocities were set equal to corresponding values one grid point inside the lower boundary. These nonuniform exit velocities were integrated to obtain a total mass flux. Similar to Srinivasan et al (Ref. 6) and Strawn and Barth (Ref. 20), the boundary condition at the inflow regions was approximated using the velocity produced by a sink at the center of rotation. Instead of basing the sink strength on the rotor thrust, however, the strength was set equal to the aforementioned mass flux. Mass conservation through the far-field boundary was therefore preserved and reliance on momentum theory to specify the exit velocity was avoided. Additional details are found in Yamauchi (Ref. 18).
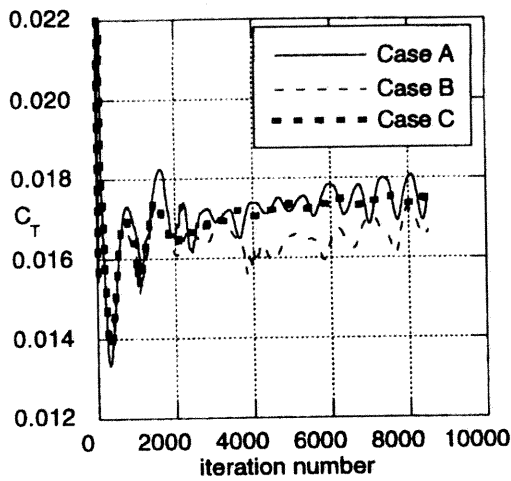
Effect of Boundary Conditions

The analysis with the modified root and far-field boundary conditions was validated using hover data from a model prop rotor (Yamauchi and Johnson (Ref. 12)). However, the effect of these modifications on performance or loads was not assessed; this assessment is provided here using a V-22 blade geometry at 16 deg of collective pitch and M_{tip} of 0.68.

All the analyses used the same grid geometry and were run out to 8500 iterations. Calculations were performed using the original two-dimensional root boundary condition with the far-field inflow boundary condition based on momentum theory; the no-slip root boundary condition with the far-field inflow boundary condition based on momentum theory; and the no-slip root boundary condition with far-field inflow boundary condition based on mass conservation. For all cases, the exit velocities at the lower boundary were set equal to corresponding values one grid point inside the lower boundary; therefore, none of the cases correspond exactly to the method reported in Srinivasan et al (Ref. 6).

493

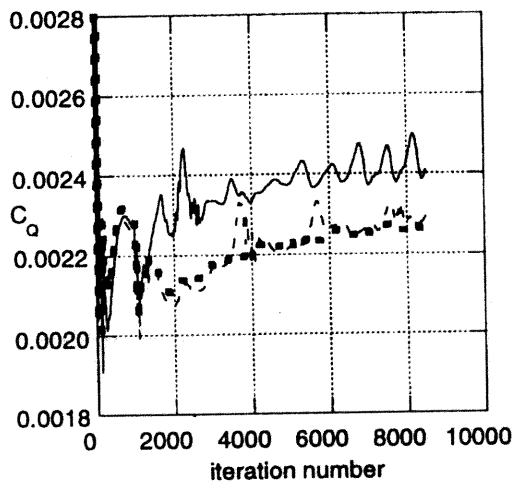Table 1. Effect of Boundary Conditions on V-22 Performance

Boundary Condition Case	C_T	C_Q	FM
Case A. 2D root boundary condition; far-field inflow boundary condition based on momentum theory	0.01754	0.002421	0.68
Case B. No-slip root boundary condition; far-field inflow boundary condition based on momentum theory	0.01674	0.002288	0.67
Case C. No-slip root boundary condition; far-field inflow boundary condition based on mass conservation	0.01745	0.002261	0.72

a) rotor thrust coefficient
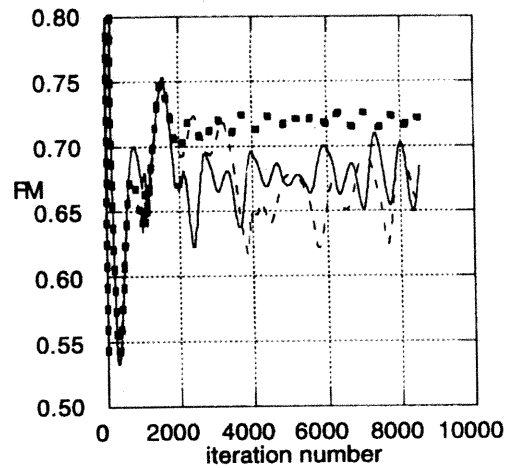
c) figure of merit

b) rotor torque coefficient
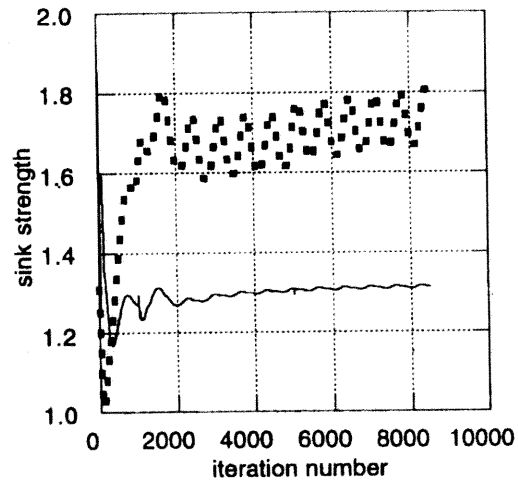
d) sink strength

Figure 4. Effect of boundary conditions on performance and sink strength (V-22 twist, collective=16 deg, $M_{tip}=0.68$).

494

a) section thrust coefficient

b) section torque coefficient
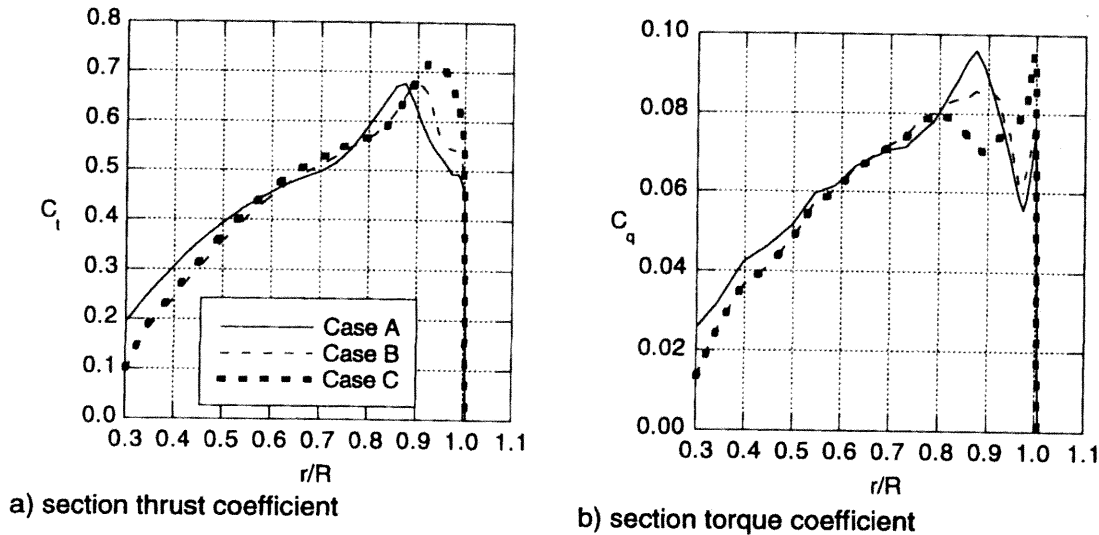
Figure 5. Effect of boundary conditions on spanwise loads (V-22 twist, collective=16 deg, M_{tip}=0.68)

Table 1 shows values of C_T, C_Q, and FM obtained by calculating the average of values between the 7000th and 8500th iteration for the three boundary condition cases.

Compared with Case A, Case B produces a lower C_T and C_Q, resulting in a FM value within one count (0.01) of Case A. Case C, however, produces approximately the same amount of thrust as Case A, but a lower C_Q resulting in a noticeably higher FM compared with Case A. Figure 4 shows the behavior of C_T, C_Q, FM, and sink strength with solution iteration. Adding the far-field boundary condition based on mass conservation dampens the oscillatory behavior of the loads with iteration (compare Case B and Case C in Figs. 4a)-c)). Figure 4d) compares the sink strength computed from momentum theory and from mass conservation. The sink strength based on mass conservation is larger than the strength based on momentum theory, which produces larger inflow velocities at the far-field.

The spanwise variation of C_t and C_q are presented in Figs. 5a) and b), respectively. Figure 5a) shows the no-slip root boundary condition (Case B) causes the thrust generated by the inboard 60 percent of the blade to decrease (compare Case A and Case B); there is a slight gain in thrust produced at the tip compared with Case A. Adding the far-field boundary condition based on mass conservation (Case C) creates a large gain in thrust produced near the tip, which offsets the inboard thrust loss, resulting in a C_T comparable to Case A (see Table 1). Figure 5b) shows that compared to Case A, the C_q for Cases B and C decreases for r/R<0.60. For r/R>0.60, C_q distribution is quite different for Case C compared with Cases A and B.

The no-slip boundary condition at the root and the far-field inflow boundary condition based on mass conservation together produced noticeable effects on calculated section loads and performance. Although these boundary conditions were still approximations, they provided a more physical representation of the flow field boundaries than the two-dimensional root boundary condition and the far field inflow boundary condition based on momentum theory. Therefore, results presented in the remaining sections of this paper were calculated using the no-slip boundary condition at the root and the far-field inflow boundary condition based on mass conservation (Case C).

PREVIOUS VALIDATION STUDY

Before proceeding with the investigation of blade twist effects on tilt rotor flow fields, a validation study (Yamauchi and Johnson (Ref.12)) was performed using the analysis described in the present paper and data from a model prop rotor. Calculations were compared with measured hover performance, surface pressures, and wake geometry. The study found that differences in calculated and measured figure of merit ranged from less than one percent at low thrust to 7 percent at high thrust. This level of difference is comparable to results from previous helicopter rotor performance validation studies. For both low and high thrust levels, differences between calculated and measured section normal force coefficient and surface pressures decreased with increasing radial station, with good agreement at the most outboard measured station (0.75R). The study also showed fair correlation with measured wake geometry, although calculated tip vortex descent rate and contraction rate were initially less than the measured rates. Based on the results of

495

Ref. 12, the analysis was determined to be sufficient for investigating highly-twisted rotors.

RESULTS

The overall objective of this investigation is to understand how the physical features of a tilt rotor blade and conventional helicopter blade influence the blade fluid dynamic environment. Understanding the differences in the fluid dynamics of the two types of blades will explain why tilt rotor blades have better hover performance than helicopter blades at high thrust levels. Varying blade twist, while keeping other physical features constant, was selected as the approach for addressing the objective of this study.

In this section, calculations are first compared with performance data from a 0.658-scale model of the V-22 (Felker, Signor, Young, and Betzina (Ref. 20)). There were no full-scale tilt rotor blade pressure data in the literature, so the comparisons with measurements were limited to performance. Next, using full-scale V-22 geometry, changes in performance, section loads, flow separation location, tip vortex formation, and other fluid dynamic phenomena as the blade twist was systematically changed from that of a tilt rotor to a helicopter (small linear twist) are presented.

Since the grid generation code was a single-block type, the center spinner was not modeled. The V-22 blade has a root fairing which extends from 0.09R to 0.25R. Using a root cut-out of 0.09R was not possible because of the grid generator limitations discussed earlier. For this study, the first spanwise grid station was placed at 0.23R, which corresponds to the first airfoil section on the actual blade. This was a loss of 0.14R worth of blade material and must be considered when comparing measured and calculated thrust.

Comparison with Experimental Data

As presented in Felker et al (Ref. 21), hover performance data from a 0.658-scale model of a V-22 tilt rotor were acquired at the Outdoor Aerodynamic Research Facility at NASA Ames Research Center. The three-bladed tilt rotor model was 25 ft in diameter (the full-scale V-22 is 38 ft in diameter). The 0.658-scale rotor had a greater solidity (0.1138) compared with the full-scale rotor (0.105). The increase in solidity was achieved by increasing the blade chord by 8.4 percent everywhere along the span. The tilt rotor shaft axis was mounted horizontally with the shaft centerline 1.76 rotor radii above the ground.

Data for winds less than 1.5 m/s were selected for comparison with the calculations. The tip Mach number for the data was 0.68, which gives a Reynolds number based on the chord at 0.75R of 7.20×10^6. The blade grid geometry included the 8.4 percent increase in chord along the span.

Calculations were run for different collective settings which covered the majority of the thrust range of the experimental data. The solution was run for 8500 iterations; the first 1000 iterations were run using every other grid point. The residual was reduced by 2 orders of magnitude, then oscillated about a mean value. Similarly, C_T eventually oscillated about a mean value. The 16 deg case was run an additional 4000 iterations; no significant difference between the solution at 8500 and 12500 iterations was observed. Therefore, the remaining cases were run to 8500 iterations to conserve computer time. Figure 6 compares measured and calculated hover performance. The C_T, C_Q, and FM values were obtained by computing the average values from the 7000th to 8500th iteration.
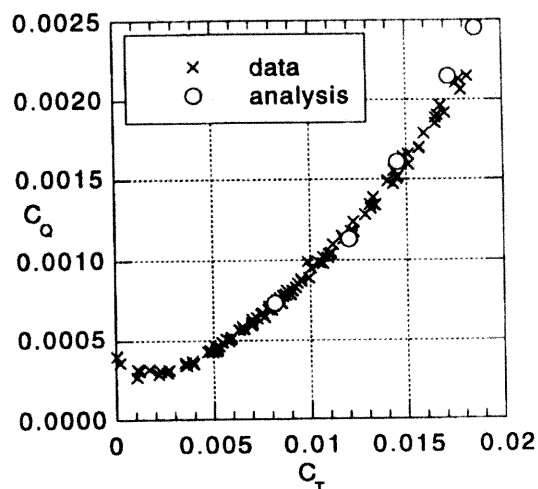
a) rotor torque coefficient
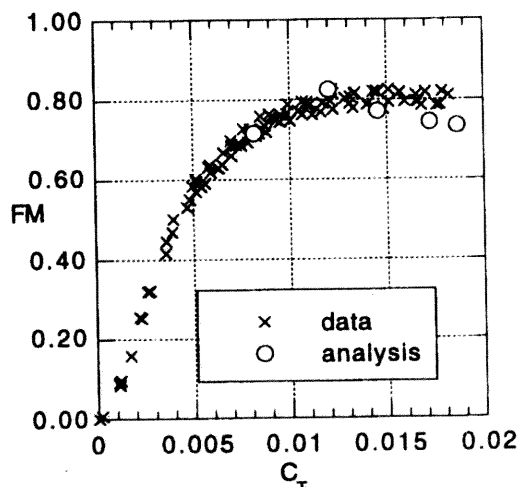
b) figure of merit

Figure 6. 0.658-scale V-22 hover performance.

The analysis generally predicts (within approximately one percent) FM at the lowest thrust levels, but underpredicts (up to 10 percent) the FM at the highest thrust levels. Unlike the experimental data, the calculations show the rotor has stalled at approximately C_T=0.014.

Effect of twist variation on tilt rotor flow fields

An analysis of full-scale tilt rotor results progressing from general to specific follows next. First, gross performance characteristics are discussed, followed by an examination of spanwise loads and skin friction coefficient. The vorticity in the flow field surrounding the blade is also discussed.

Performance. The conditions for these cases are: M_{tip}=0.68 and Reynolds number (based on full-scale chord 0.75R)=10.1×10^6. All cases were run out to 8500 iterations.

Figure 7 shows the twist schedule for the cases examined. The cases of specific interest were the V-22 twist (Case 2) and a -10 deg linear twist (Case 8). The intermediate twist distributions were obtained by combining the V-22 and linear twist in varying amounts. For example, the twist angle at a given radial location for Case 3 was obtained by adding 97% of the V-22 twist value and 3% of the linear twist value at that station.

For comparison purposes, the collective pitch of each case was adjusted iteratively so that the resulting thrust coefficient for all eight cases was approximately the same. Table 2 shows the computed C_T, C_Q, and FM for each case. As described earlier, the values were obtained by averaging over the 7000th to 8500th iteration. Table 2 clearly shows the effect of twist on FM and therefore stall. Table 2 also suggests that distributions with more inboard pitch than the V-22 (Case 1) can provide better hover performance.
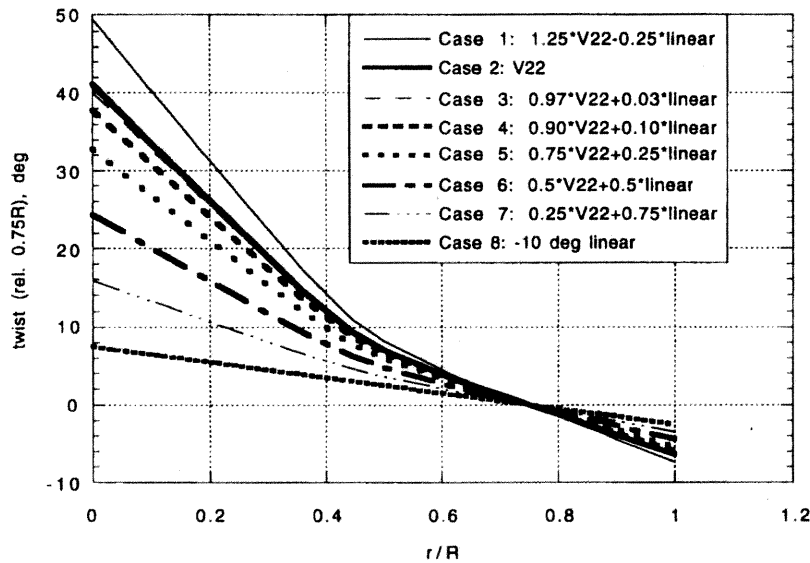

Figure 7. Distributions for twist effect study.

Table 2. Performance Values for Twist Variation Cases

Case	Twist type	collect. (deg)	C_T	C_Q	FM
1	1.25*V-22-0.25*linear	15	0.01760	0.002122	0.78
2	V-22	16	0.01745	0.002261	0.72
3	0.97*V-22+0.03*linear	16.5	0.01731	0.002449	0.66
4	0.90*V-22+0.10*linear	17	0.01787	0.002608	0.65
5	0.75*V-22+0.25*linear	17	0.01749	0.002588	0.63
6	0.50*V-22+0.50*linear	17.5	0.01781	0.002766	0.61
7	0.25*V-22+0.75*linear	18	0.01732	0.003000	0.54
8	-10 deg linear	19	0.01732	0.003217	0.50

497

Spanwise Loads. The spanwise loading for Cases 1-8 is examined next. Figure 8 shows the spanwise variation of section thrust coefficient, C_t (normal to the rotor plane). Cases 1 and 2 show the maximum C_t is slightly beyond 0.90R. As the twist distribution is driven toward the linear twist, the peak in C_t moves inboard. The peak for Case 8, however, appears slightly outboard compared with Case 7; this is discussed later. Note that Case 3 has only a slightly different twist distribution than the V-22 twist (Case 2), but shows a very different C_t distribution. In fact, Case 3 (along with Cases 4-8) show signs of possible vortex interaction at the tip. The vortex location is discussed later.
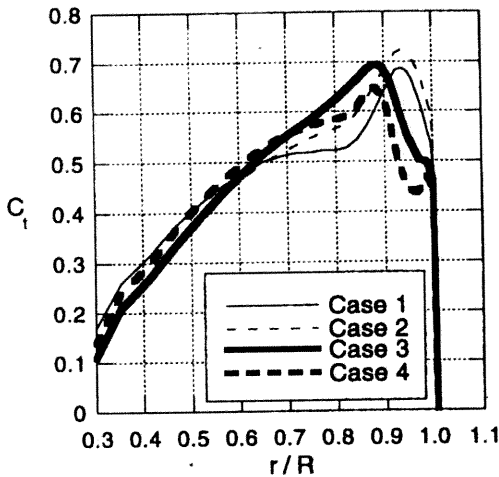
The in-plane force coefficient, C_x, is shown in Fig. 9. Transforming the tilt rotor twist into a linear twist distribution increases the in-plane force coefficient significantly near the blade tip. If C_x is multiplied by the blade radial station, the section torque (C_q) coefficient is obtained (see Fig. 10). If the C_q distributions in Fig. 10 are integrated over the blade, the rotor torque coefficient is obtained. Therefore, the differences in C_x at the tip have more influence on rotor performance (i.e. figure of merit) than differences further inboard on the blade. The increase in C_x near the tip explains why the figure of merit (Table 2) decreases as the twist becomes more linear.
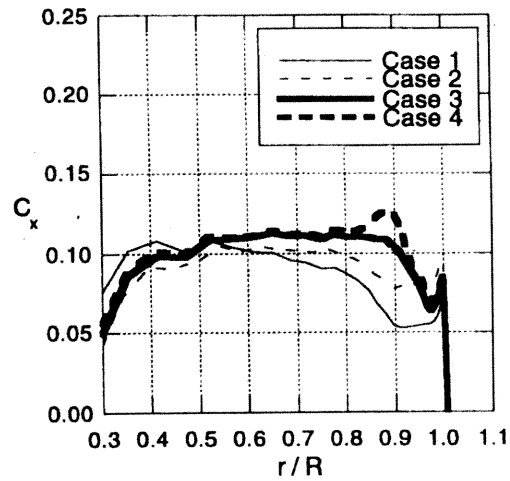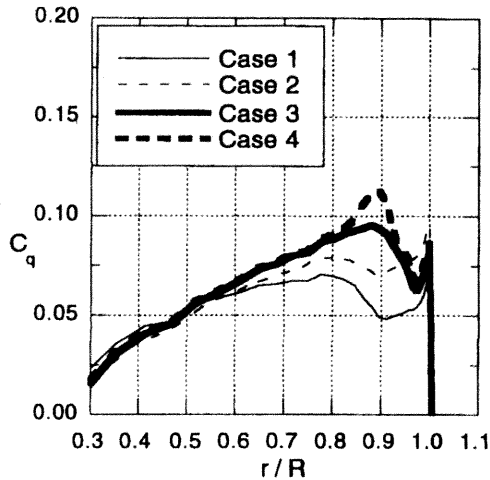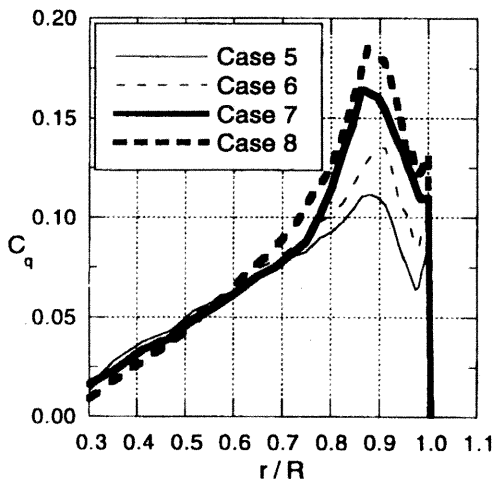

a) Cases 1-4
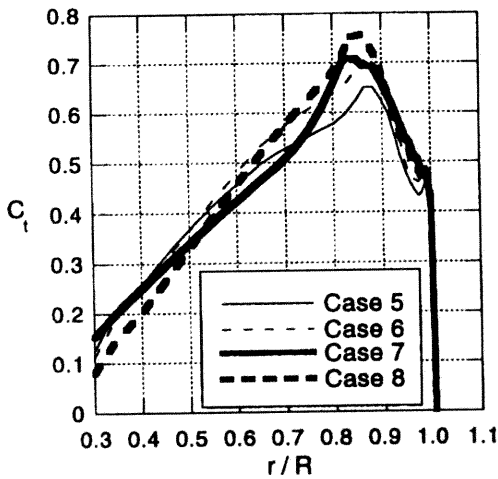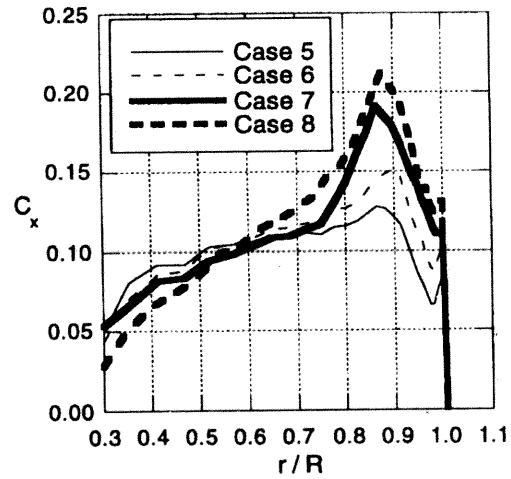
b) Cases 5-8

Figure 8. Effect of twist on section thrust coefficient.

a) Cases 1-4

b) Cases 5-8

Figure 9. Effect of twist on section in-plane force coefficient.

498

a) Cases 1-4

b) Cases 5-8

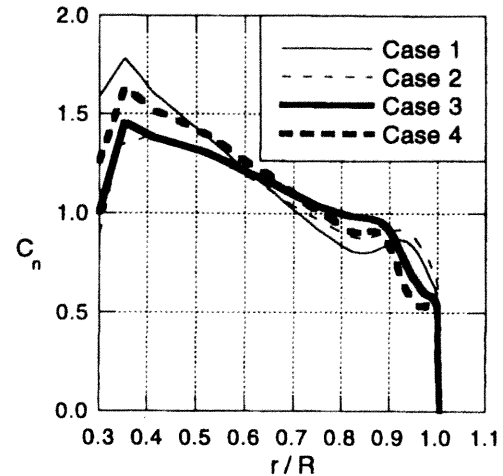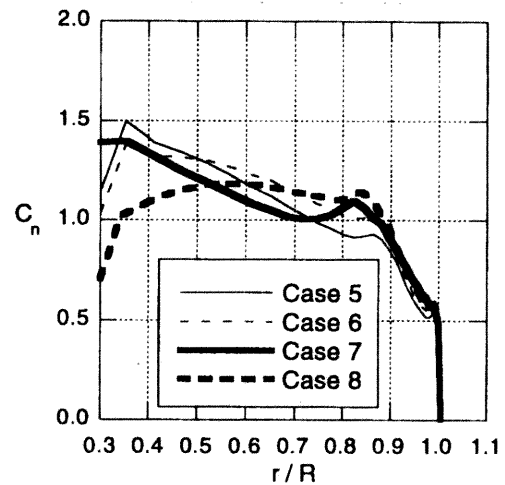Figure 10. Effect of twist on section torque coefficient.

a) Cases 1-4

b) Cases 5-8

Figure 11. Effect of twist on section normal force coefficient.

The normal force coefficient is presented in Fig. 11. C_n is defined as normal to the local blade chord. As with the C_t distribution, the C_n curve contains a small bump outboard of 0.80R. The peak of the bump moves inboard as the twist becomes more linear. Also, Case 8 (-10 deg linear twist) clearly shows a reduction in C_n at the inboard stations, while Cases 1-7 maintain a relatively high value for C_n. The approximate root boundary condition may be the cause of the decrease in C_n as the root is approached.

The two-dimensional maximum lift coefficient for the airfoil section between 0.10R and 0.45R is approximately 1.3-1.4. If the C_n values of Fig. 11 are assumed to approximate the section lift coefficient, then the two-dimensional maximum lift coefficient for the airfoil section for r/R<0.45R is equaled or exceeded by Cases 1-7, but not to a large extent. A very large inboard lift coefficient might be expected, based on observations of wind turbine and propeller behavior at high thrust levels (see Corrigan and Schillings (Ref. 22) for a comprehensive review of this topic); however, this is not the case for the tilt rotor geometry studied here.

499

Comparing lift coefficients from two-dimensional nonrotating flows and 3D rotating flows is difficult, since the induced velocity in 3D rotating flows is not known and not included in nondimensionalizing the section normal force.

The loading for Cases 2 and 8 is examined next to insure the analysis is consistent throughout a range of thrust levels. Figure 12 presents the effect of thrust levels on section normal force for Case 2 (V-22 twist) and Case 8 (-10 deg linear twist).
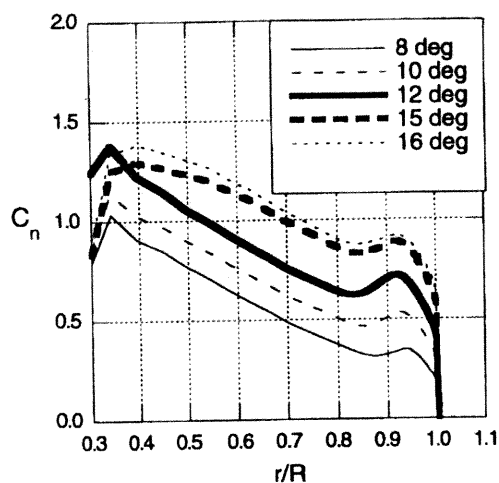
a) Case 2: V-22 twist
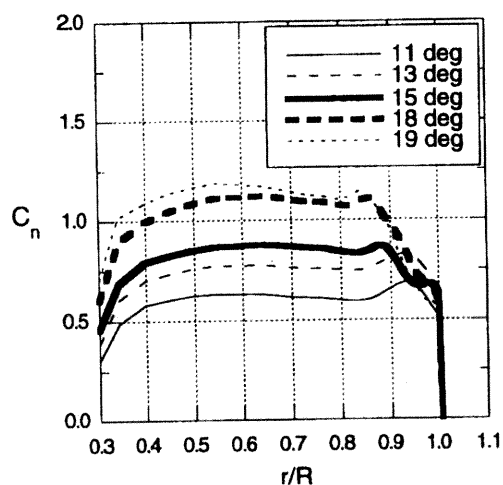
b) Case 8: -10 deg linear twist

Figure 12. Effect of thrust on normal force coefficient.

Note that as the thrust level increases for the linear twist case, the C_n value decreases near the tip and the peak

C_n moves inboard (Fig. 12b)). Contrast this behavior with Fig. 12a) for the V-22 twist. There is some inboard movement of the peak C_n value, but certainly not as large as the linear twist case. At the highest thrust level for the linear twist case, the outer 10% of the blade is not nearly as productive in generating lift compared to the V-22 blade.

Figure 13 and 14 present the effect of thrust on the C_t and C_x distributions, respectively. The trends for the V-22 and linear twist cases are similar to the C_n behavior of the previous figure, i.e., there is a smooth progression from low to high thrust levels. In Fig. 14b), the large increase in C_x near the blade tip as the collective is increased from 15 to 19 deg indicates the onset of stall. Figures 12-14 reveal that the load distributions computed by the analysis are consistent throughout a range of thrust levels. The performance correlation with the 0.658-scale data showed that the analysis generally predicted FM at the lowest thrust levels, but underpredicted the FM at the highest thrust levels. Based on the results presented in this section, the underprediction is most influenced by the behavior at the tip, not the root. Overpredicting the amount of separation, and therefore the drag, at the tip will degrade the prediction much more than an underprediction of the inboard lift. The magnitude of the separated region predicted by the analysis can be questioned because of the simple turbulence model used, but this should not undermine the validity of the trends seen in the twist and thrust sweeps.

Skin Friction. Figure 15 shows blade upper surface skin friction (C_f) vectors for Cases 2 and 8 for thrust conditions listed in Table 1; every other grid point is shown for clarity. Case 2 shows the flow is well-behaved until approximately 0.88R. From 0.88R to 0.92R, the C_f vectors (and hence the velocities) become very small. Determining the cause for this pocket of low velocity requires analysis of the flow region surrounding the blade. As the twist is reduced to the -10 deg linear case (Case 8), the flow at the leading edge beyond 0.89R is no longer completely chordwise, indicating flow separation (or at the very least, some type of flow instability). In addition, signs of spanwise flow appear near the trailing edge. The area of spanwise flow spreads from the trailing edge to leading edge and moves further inboard as the twist becomes more linear. Skin friction results for the inboard regions of Cases 1-8 revealed well-behaved flow (Yamauchi (Ref. 18)).
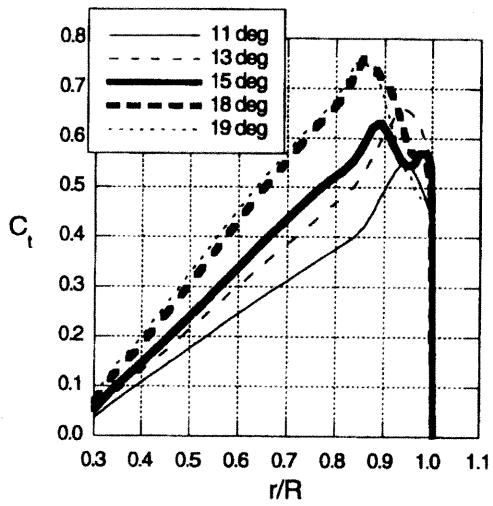
To verify whether the flow is indeed separated at the outboard stations, vorticity contours are examined next.
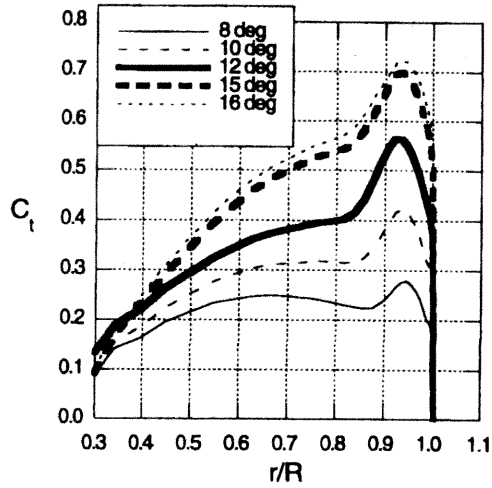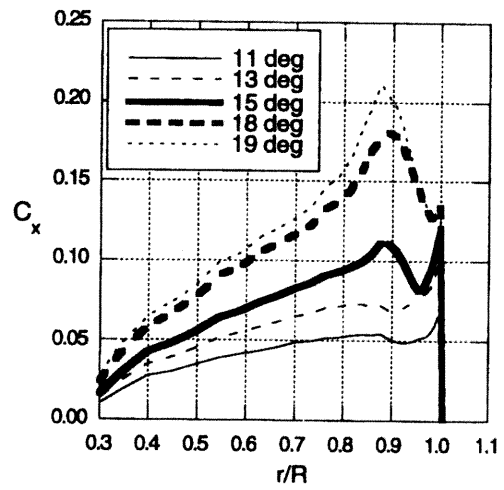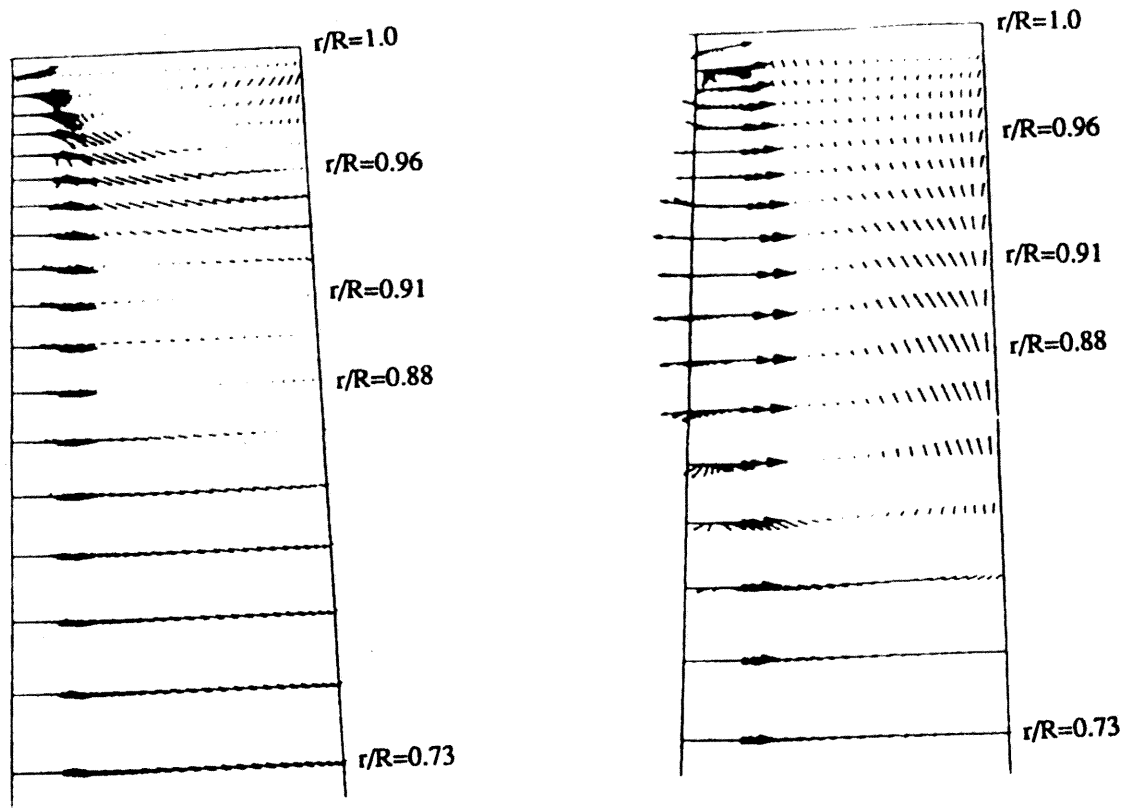
a) Case 2: V-22 twist
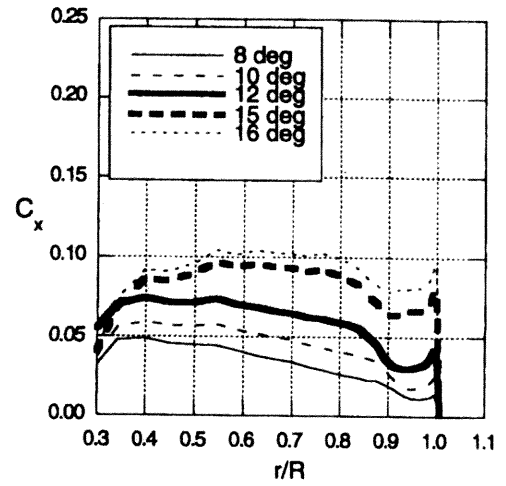
b) Case 8: -10 deg linear twist

Figure 13. Effect of thrust effect on section thrust coefficient

a) Case 2: V-22 twist

b) Case 8: -10 deg linear twist

Figure 14. Effect of thrust on section in-plane force coefficient.

a) Case 2: V-22 twist

b) Case 8: -10 deg linear twist

Figure 15. Effect of twist on blade outboard upper surface skin friction coefficients; every other grid point shown (M_{tip}=0.68, nominal C_T=0.0175)

Vorticity Contours. The next level of detail requires examining the flow around the blade to determine what is causing the spanwise flow and separation at the blade surface. Figure 16 shows the flow field for a plane approximately 0.5 chords upstream of the leading edge. Cases 2 shows a much tighter vortex from the previous blade than does Case 8. A second, weak vortical structure is also seen below the blade for all cases, although this second vortex is highly distorted for Case 8. The location of the first vortex appears below the rotor plane, as expected, for Case 2. For Cases 8, however, the vortex is either in the plane of the rotor or above. This is not expected. Before exploring the reason for this behavior, additional slices through the flow field for Cases 2 and 8 will be addressed. Figure 17 presents results for a plane located approximate mid-chord. Both cases show that the

tip vortex has begun to form. In addition, Case 8 shows that the vortex structure from the previous blade located above (or in) the rotor plane has now interacted with the separated flow region on the blade, resulting in a region of very high vorticity above the blade near the tip. Case 2, however, shows that the vortex structure from the previous blade remains relatively intact, with some distortion occurring from the separated flow region on the blade upper surface. As the solution plane is moved downstream to the blade trailing edge, Fig. 18, Case 2 shows three distinct vortical structures: two (albeit one weak structure) below the rotor blade and the tip vortex. Case 8, however, indicates that the vortical structure that was above (or in) the rotor plane (Fig. 16b)) has been distorted by the additional vorticity in the separated flow region; also, discerning three vortical structures is not

502

easy. There is also the question of how the newly formed tip vortex in Fig. 18 for Case 8 is prevented from descending below the rotor plane. Spanwise cuts of the flow field showing vorticity components may help uncover an explanation for the distorted flow fields.

Before proceeding to the discussion of the spanwise cuts through the solution field, a check of the flow field features for a much lower thrust level for the Case 8 geometry is in order. At low thrust levels, attached flow is expected over the majority of the blade and the tip vortices should descend below the rotor plane within one blade passage. This behavior is confirmed by series of chordwise cuts through the solution field shown in Fig. 19. The thrust coefficient is 0.0106. Comparing Figs. 19a) and b) with Figs. 16b) and 18b), the vortical structure from the preceding blade is much tighter and identifiable for the low thrust case than the high thrust case. Based on this comparison, the conclusion is made that the separated flow of the high thrust case is influencing the position and formation of the tip vortex, rather than the cause being an error or deficiency in the computed results.

Figure 20 presents spanwise cuts through the flow field showing contours of the y-component of vorticity (positive direction of y-vorticity is defined as being from root to tip) for both Case 2 (V-22 twist) and Case 8 (linear twist). In Fig. 20, high concentrations of positive and negative vorticity are indicated by a '+' and '-', respectively. At r/R=0.91R (Fig. 20a)), Case 8 shows separation has occurred at the leading edge, resulting in positive y-vorticity being discharged into the flow field. In addition, there is some negative y-vorticity being shed from the trailing edge. Case 2 reveals the separated region

is very thin until a shock is encountered slightly downstream of the leading edge, after which separation occurs. At r/R=0.96 (Fig. 20b)), Case 8 shows the separation region encompasses more of the leading edge. Case 2, however, still shows no sign of massive separation; the separated layer at this radial station is thinner than at 0.91R. Moving further outboard to 0.99R (Fig. 20c)), Case 8 shows that the flow has separated over the first half of the airfoil. Separation appears to have occurred for Case 2 slightly downstream of the leading edge. At r/R=1.0 (Fig. 20d)), the formation of the tip vortex adds to the already nonuniform flow field of Case 8. The separation region for Case 2 now extends over the first half of the airfoil. For Case 8, the high level of y-vorticity spread over a large region near the tip induces an upwash in front of the blade. This induced upwash affects the position of the oncoming tip vortex shed from the previous blade. Indeed, for Case 8, the oncoming tip vortex is greatly distorted because of the interaction with the separated flow during and after the tip vortex formation, and also by the induced upwash after one blade passage. By viewing Fig. 20 together with the C_f plots (Fig. 15), reasons for the changing C_f vector direction can be gleaned.

The shock-like feature identified in Fig. 20 for Case 2 is highlighted by examining Mach number contours for r/R=0.91 (Fig. 21). The contours represent Mach number magnitudes in the inertial frame. With $M_{tip}=0.68$, the blade-fixed contour level corresponding to the maximum inertial frame level is approximately 1.5. Hence, the shock in Fig. 21 is quite strong and causes separation. Note that the flow field for Case 8 shows no sign of shock behavior.
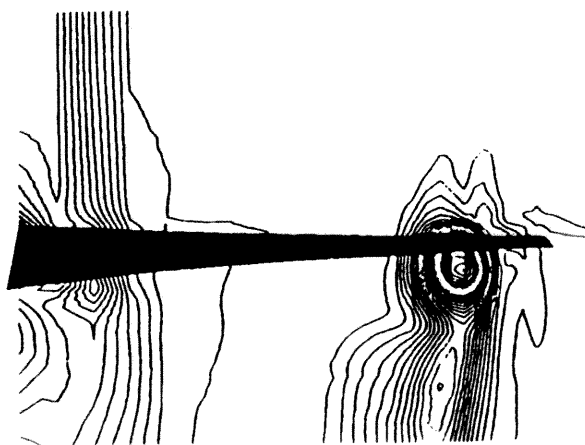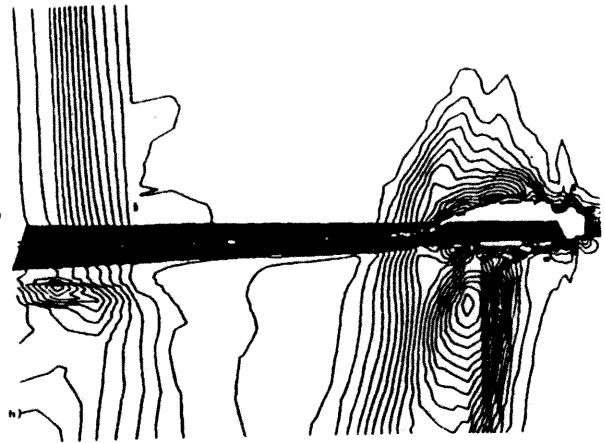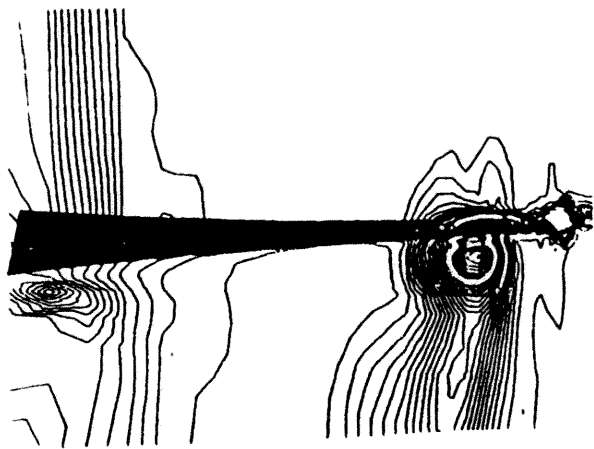

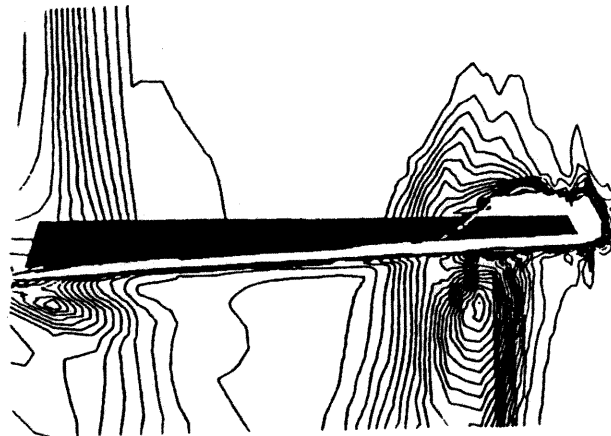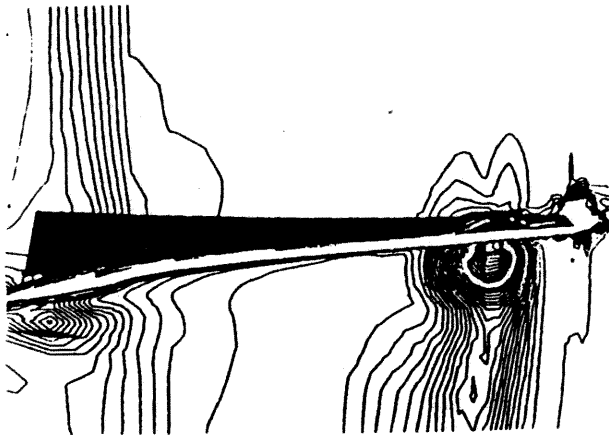a) Case 2: V22 twist
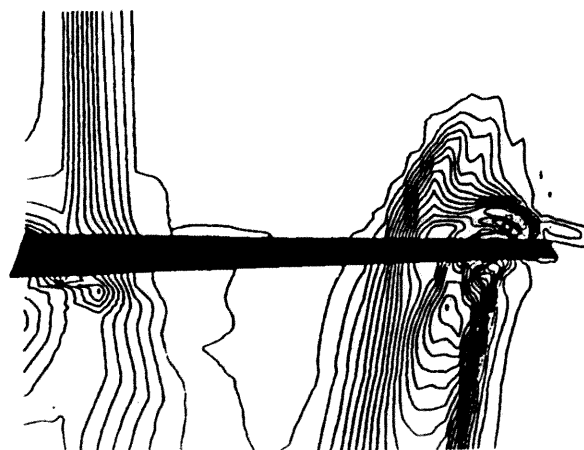
b) Case 8: -10 deg linear twist

Figure 16. Effect of twist on vorticity magnitude in a plane 0.5 chords upstream of the blade leading edge ($M_{tip}=0.68$, nominal $C_T=0.0175$).

503

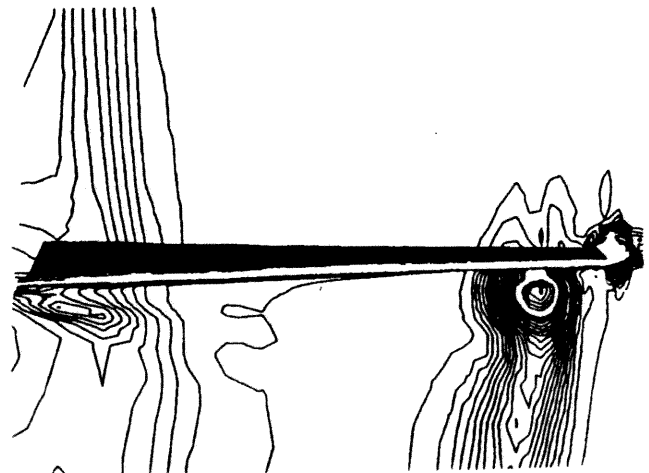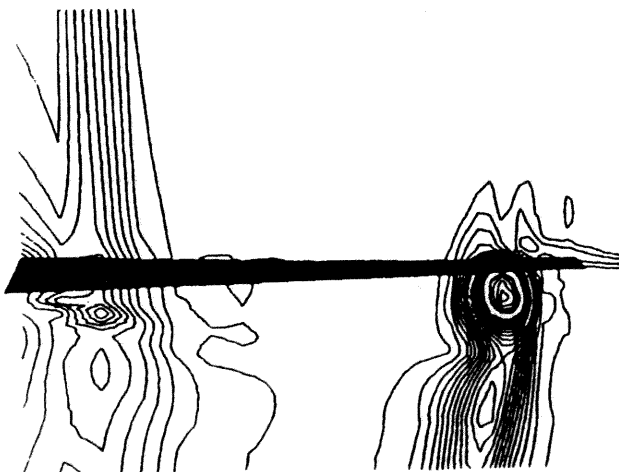a) Case 2: V22 twist   b) Case 8: -10 deg linear twist

Figure 17. Effect of twist on vorticity magnitude in a plane 0.5 chords downstream of the blade leading edge (M_{tip}=0.68, nominal C_T=0.0175).

a) Case 2: V22 twist   b) Case 8: -10 deg linear twist

Figure 18. Effect of twist on vorticity magnitude in a plane at the blade trailing edge (M_{tip}=0.68, nominal C_T=0.0175).

a) 0.5 chords upstream of blade leading edge   b) at the blade trailing edge

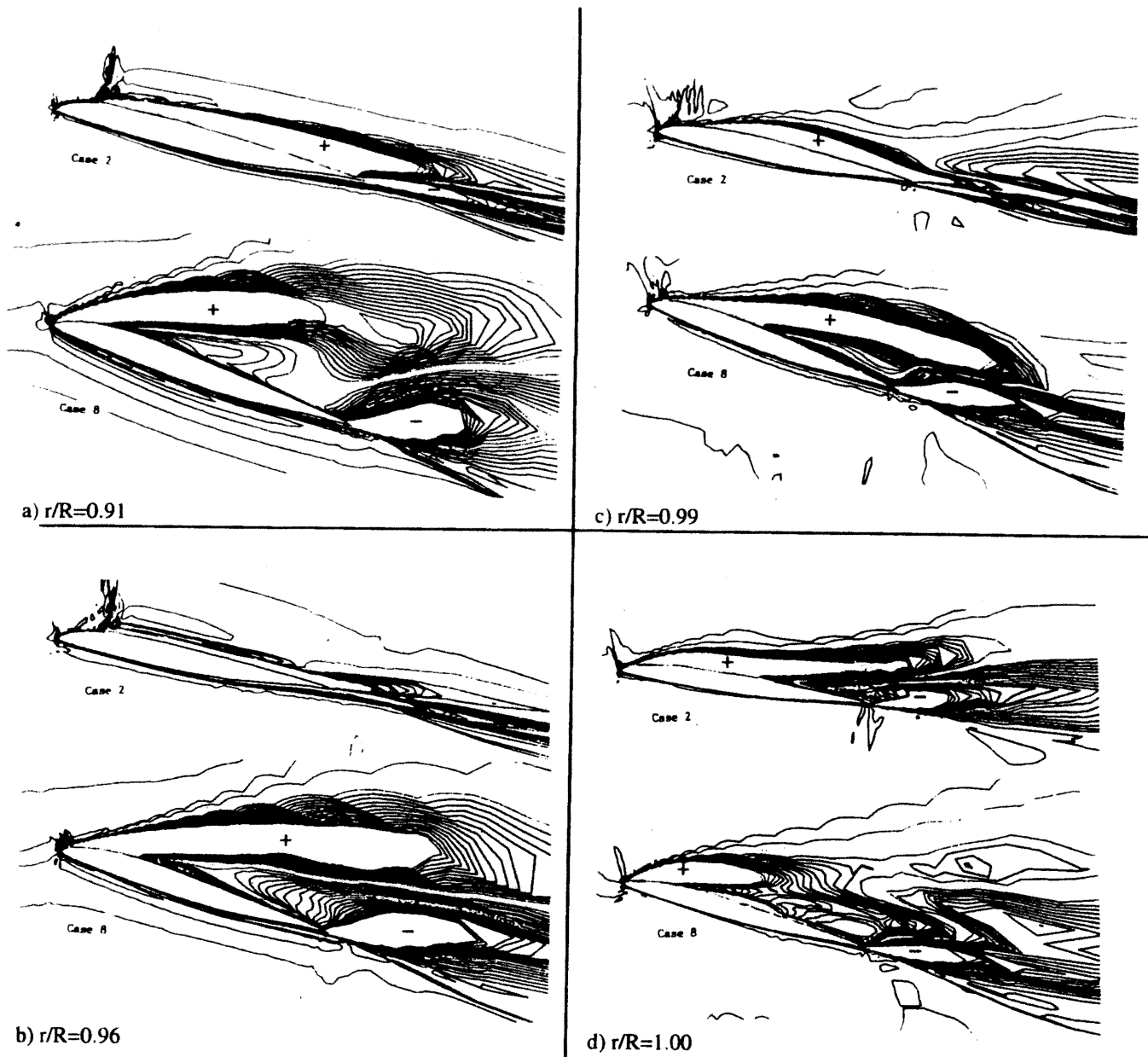Figure 19. Vorticity magnitude for Case 8 (-10 deg linear) for M_{tip}=0.68, nominal C_T=0.0106.

a) r/R=0.91

b) r/R=0.96

c) r/R=0.99

d) r/R=1.00

Figure 20. y-vorticity contours for the Case 2 (V22 twist) and Case 8 (-10 deg linear twist) for M_{tip}=0.68, nominal C_T=0.0175.
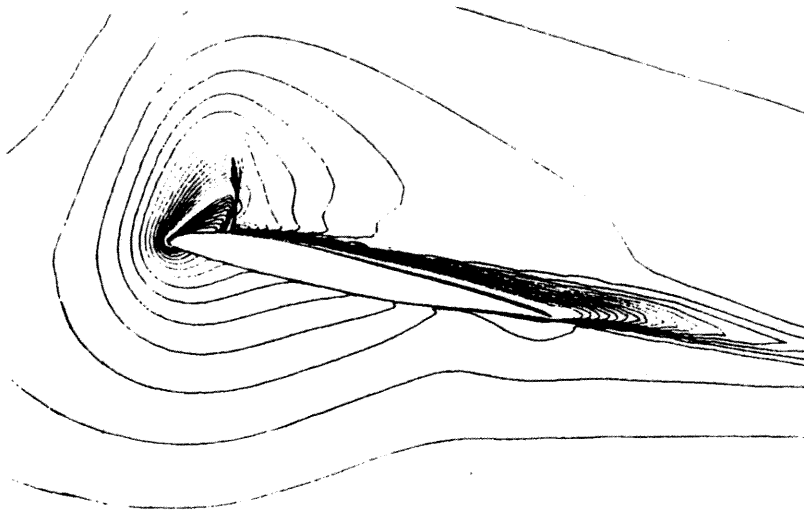
Figure 21. Mach number contours for Case 2 (V22) at r/R=0.91 (M_{tip}=0.68, nominal C_T=0.0175).

CONCLUSIONS

The flow field of highly-twisted rotors was analyzed using a thin-layer Navier-Stokes analysis. Blade root and far-field boundary conditions were investigated. A V-22 rotor with varying amounts of twist was analyzed over a range of thrust conditions. Specific findings from the investigation are discussed below.

Limitations of the single-block grid generator were encountered near the blade root when modeling the highly-twisted rotor blades. Enforcement of the periodic boundary condition caused grid cell skewing, especially when a large collective pitch was imposed; thus, the amount of collective pitch (and subsequently thrust) was limited.

The no-slip root boundary condition and the far-field inflow boundary condition based on mass conservation together produced noticeable effects on calculated section loads. This resulted in a figure of merit greater than that calculated with the two-dimensional root boundary condition and the far field inflow boundary condition based on momentum theory.

The analysis was determined to be sufficient for investigating highly-twisted rotor flow fields by validating the calculations with model prop rotor data and comparing 0.658-scale V-22 rotor performance data with calculations. Figure of merit was predicted to within one percent at the lower thrust levels with the difference increasing to 10 percent at the highest thrust level analyzed. In addition, an examination of spanwise loading as a function of thrust verified the analysis was consistent.

The study of twist effects on stall behavior of a full-scale V-22 blade suggested that separation on the linearly twisted blade was closely coupled with the tip vortex. Separation on the highly-twisted tilt rotor blade was shock-induced. As the twist was changed from a tilt rotor blade twist to a conventional helicopter blade twist, while maintaining thrust, the separated region near the tip grew. This caused the section in-plane force near the tip to increase significantly, which caused the rotor torque to increase, resulting in degraded performance. The flow in the blade inboard region (r/R< 0.50) remained attached and well-behaved for all twist cases and thrust conditions analyzed. The twist variation study suggested that distributions with more inboard pitch than the V-22 can provide better hover performance.

ACKNOWLEDGEMENTS

REFERENCES

1. Strawn, R. C. and Caradonna, F. X., "A Conservative Full-Potential Model for Unsteady Transonic Rotor Flows," *AIAA Journal*, Vol. 25, (2), February 1987.

2. Chen, C. L., McCroskey, W. J., and Ying, S. X., "Euler Solution of Multiblade Rotor Flow," Thirteenth European Rotorcraft Forum, Arles, France, September 1987.

3. Srinivasan, G. R. and McCroskey, W. J., "Navier-Stokes Calculations of Hovering Rotor Flow fields," Journal of Aircraft, Vol. 25, (10), October 1988. (AIAA Atmospheric Flight Mechanics Conference, AIAA Paper No. 87-2629-CP, Monterey, CA, August 1987).

4. Narramore, J. C. and Vermeland, R., "Use of Navier-Stokes Code to Predict Flow Phenomena Near Stall as Measured on a 0.658-Scale V-22 Tiltrotor Blade," AIAA 20th Fluid Dynamics, Plasma Dynamics, and Lasers Conference, AIAA Paper No. 89-1814, Buffalo, NY, June 1989.

5. Srinivasan, G. R., Baeder, J. D., Obayashi, S., and McCroskey, W. J., "Flowfield of a Lifting Hovering Rotor - A Navier-Stokes Simulation," Sixteenth European Rotorcraft Forum, Glasgow, Scotland, September 1990.

6. Srinivasan, G. R., Raghavan, V., and Duque, E-P. N., "Flowfield Analysis of Modern Helicopter Rotors in Hover by Navier-Stokes Method," International Technical Specialists Meeting, Rotorcraft Acoustics and Rotor Fluid Dynamics, Philadelphia, PA, October 1991.

7. Wake, B. E. and Baeder, J. D., "Evaluation of the TURNS Analysis for Hover Perfomance Prediction," American Helicopter Society Aeromechanics Specialists Conference, San Francisco, CA, January 1994.

8. Tung, C. and Lee, S., "Evaluation of Hover Performance Prediction Codes," 50th Annual National Forum of the American Helicopter Society, Washington, D. C., May 1994.

9. Ramachandran, K., Owen, S. J., Caradonna, F. X., and Moffitt, R. C., "Hover Performance Prediction Using CFD," 50th Annual National Forum of the American Helicopter Society, Washington, D. C., May 1994.

10. Meakin, R., "Unsteady Simulation of the Viscous Flow About a V-22 Rotor and Wing in Hover," AIAA Atmospheric Flight Mechanics Conference, AIAA Paper No. 95-3463, Baltimore, MD, August 1995.

11. Kocurek, J. D., Berkowitz, L. F., and Harris, F. D., "Hover Performance Methodology at Bell Helicopter Textron," 36th Annual Forum of the American Helicopter Society, Washington, D. C., May 1980.

12. Yamauchi, G. K. and Johnson, W., "Flow Field Analysis of a Model Prop Rotor in Hover," Twenty-First European Rotorcraft Forum, St. Petersburg, Russia, August/September 1995.

13. Pulliam, T. H. and Steger, J. L., "Implicit Finite-Difference Simulations of Three-Dimensional Compressible Flow," *AIAA Journal*, Vol. 18, (2), February 1980.

14. Srinivasan, G. R., McCroskey, W. J., Baeder, J. D., and Edwards, T. A., "Numerical Simulation of Tip Vortices of Wings in Subsonic and Transonic Flows,"

AIAA/ASME 4th Fluid Mechanics, Plasma Dynamics and Lasers Conference, AIAA Paper No. 86-1095, Atlanta, GA, May 1986.

15. Srinivasan, G. R. and McCroskey, W. J., "Navier-Stokes Simulations of Tip Vortices for Fixed and Rotating Helicopter Blades," International Symposium on Computational Fluid Dynamics, Sydney, Australia, August 1987.

16. Obayashi, S., "Numerical Simulation of Underexpanded Plumes Using Upwind Algorithms," AIAA Atmospheric Flight mechanics Conference, AIAA Paper No. 88-4360-CP, Minneapolis, MN, August 1988.

17. Yamauchi, G. K. and Johnson, W., "Navier-Stokes Calculations for a Highly-Twisted Rotor Near Stall," American Helicopter Society Aeromechanics Specialists Conference, San Francisco, CA, January 1994.

18. Yamauchi, G. K., "Flow Field Analysis of Highly-Twisted Rotors in Hover," Ph.D. Dissertation, Stanford University, December 1995.

19. Fujii, K. and Obayashi, S., "Navier-Stokes Simulations of Transonic Flows over a Wing-Fusleage Combination," *AIAA Journal*, Vol. 25, (12), December 1987.

20. Strawn, R. C. and Barth, T. J., "A Finite-Volume Euler Solver for Computing Rotary-Wing Aerodynamics on Unstructured Meshes," *Journal of the American Helicopter Society*, Vol. 38, (2), April 1993.

21. Felker, F. F., Signor, D. B., Young, L. A., and Betzina, M. D., "Performance and Loads Data from a Hover Test of 0.658-Scale V-22 Rotor and Wing," NASA TM 89419, April 1987.

22. Corrigan, J. J. and Schillings, J. J., "Empirical Model for Stall Delay Due to Rotation," American Helicopter Society Aeromechanics Specialists Conference, San Francisco, CA, January 1994.